East European Journal of Physics. 3. 596-607 (2026)
DOI:10.26565/2312-4334-2026-3-55 ISSN 2312-4334

COMPARATIVE ANALYSIS OF INCOMPLETE IONIZATION EFFECTS IN P-SiC/n-Ga_2O_3 AND P-GaN/n-Ga_2O_3 HETEROJUNCTIONS OVER 77–400 K

O.A. Sattarova[1], M.Sh. Ibragimova[2]*, A.Kh. Choriev[3], A. Abdukarimov[4], Jurabek Kamolov[5]
[1]Urgench State Medical Institute, 220100, Al-Khorezmi Street 28, Urgench, Uzbekistan
[2]Urgench State University, Hamid Olimjon Street, 14, Urgench, 220100 Uzbekistan
[3]National Research University TIIAME, Department of Physics and Chemistry, Tashkent, Uzbekistan
[4]Tashkent State Technical University, Tashkent, Uzbekistan
[5]Bukhara State University, Bukhara 200117, Uzbekistan
**Corresponding Author e-mail: madinabonubahodir2024@gmail.com*
Received April 8, 2026; revised June 28, 2026; accepted July 15, 2026

This study presents a comprehensive comparative investigation of wide-bandgap heterojunctions p-SiC/n-Ga_2O_3 and p-GaN/n-Ga_2O_3, with particular emphasis on the influence of incomplete dopant ionization over the temperature range of 77–400 K. The temperature-dependent bandgap energies of GaN, SiC, and Ga_2O_3 were modeled using the Varshni relation, yielding excellent agreement with reported experimental data, with correlation coefficients (R^2) of 0.981, 0.975, and 0.978, respectively. The calculated bandgaps decreased slightly with increasing temperature, varying from 3.51 to 3.40 eV for GaN, 3.33 to 3.25 eV for SiC, and 4.90 to 4.87 eV for Ga_2O_3. Corresponding heterojunction band offsets were determined to be approximately 1.36–1.50 eV for Ga_2O_3/GaN and 1.57-1.62 eV for Ga_2O_3/SiC, confirming the consistency and reliability of the adopted band-alignment model. Electric-field analysis demonstrated strong thermal robustness in both heterostructures. The maximum electric field reached 3.92×10^5 V/cm for the p-GaN/n-Ga_2O_3 heterojunction and 3.98×10^5 V/cm for the p-SiC/n-Ga_2O_3 heterojunction at 77 K, while exhibiting less than a 3% variation up to 400 K. In addition, the electric field showed a predictable dependence on doping concentration, increasing from approximately 25 kV/cm to 80 kV/cm as the doping level increased from 2×10^{14} to 2×10^{16} cm^{-3}. At room temperature, the p-GaN/n-Ga_2O_3 heterojunction exhibited slightly higher electric-field strength due to its larger conduction-band offset, whereas the p-SiC/n-Ga_2O_3 structure demonstrated enhanced low-temperature performance attributed to incomplete dopant ionization and the resulting carrier redistribution effects. The results provide new insight into the influence of incomplete dopant ionization on the temperature-dependent behavior of p-SiC/n-Ga_2O_3 and p-GaN/n-Ga_2O_3 heterojunctions, providing a theoretical basis for the design of wide-bandgap power devices. These characteristics highlight the strong potential of Ga_2O_3-based heterojunctions for next-generation high-voltage and high-temperature power electronic applications, including electric-vehicle power converters, aerospace electronics, and harsh-environment industrial systems. Nevertheless, further studies incorporating interface-state effects, breakdown-voltage analysis, leakage-current mechanisms, thermal resistance, and long-term reliability assessments are required to fully evaluate their practical device performance and optimize heterojunction design.
Keywords: *GaN; SiC; Ga_2O_3; Dopant ionization; Incomplete ionization; Cryogenic devices; Temperature effects; Ideality factors*

INTRODUCTION

Ultra-wide-bandgap (UWBG) semiconductors have become key enablers for next-generation high-power, high-frequency, and extreme-environment electronics [1,2,4-6]. Among them, gallium oxide (Ga_2O_3) stands out due to its ultra-wide bandgap (4.4–5.3 eV) and an exceptionally high theoretical critical electric field approaching 8 MV/cm. These characteristics yield a Baliga figure of merit surpassing that of conventional wide-bandgap materials such as silicon carbide (SiC) and gallium nitride (GaN) [3,7-10]. Consequently, Ga_2O_3 is highly promising for high-voltage power devices, deep-UV photodetectors, and radiation-tolerant electronics intended for aerospace, space, and harsh environmental applications [11,12].

Despite these merits, achieving reliable p-type doping in Ga_2O_3 remains a significant challenge because of large acceptor activation energies and high hole effective masses, which lead to pronounced dopant freeze-out [13–16]. This limitation restricts the fabrication of conventional p–n junctions and high-performance power devices [17,18]. Heterojunction integration, wherein n-type Ga_2O_3 is combined with well-established p-type wide-bandgap semiconductors like SiC and GaN, provides an effective strategy to overcome this constraint [19–23]. Such heterostructures not only support rectifying behavior and high current density but also improve breakdown voltage performance by leveraging the complementary properties of the constituent semiconductors [23–28].

p-Type SiC and GaN offer distinct advantages for integration with n-Ga_2O_3. SiC delivers excellent thermal and chemical stability, along with robust performance under high-voltage and radiation-intensive conditions, making it well-suited for space and harsh-environment applications [29–32]. In contrast, GaN benefits from mature epitaxial growth techniques and established Mg-based p-type doping, which ensures high hole mobility and favorable band alignment with Ga_2O_3, facilitating efficient carrier injection [33–37,41]. Accordingly, pSiC/nGa_2O_3 and pGaN/nGa_2O_3 heterojunctions constitute two practically relevant platforms whose comparative assessment is crucial for device design and optimization [38–43].

Cite as: O. A. Sattarova, M.Sh. Ibragimova, A.Kh. Choriev, A. Abdukarimov, Jurabek Kamolov, East Eur. J. Phys. 3, 596 (2026), https://doi.org/10.26565/2312-4334-2026-3-55

Temperature-dependent dopant ionization significantly influences the electrical behavior of these heterojunctions [44-50]. In UWBG semiconductors, the high activation energy of acceptors leads to incomplete ionization, particularly at low temperatures, which reduces the free carrier density and alters electric-field distribution, threshold voltage, carrier injection, and I–V characteristics [39,28,11,51]. As temperature increases from cryogenic (77 K) to room temperature (300 K), thermally activated ionization partially restores the carrier density, affecting band bending, transport mechanisms, and ideality factors [40–42]. Accurate modeling of these effects is essential for predicting device behavior across the cryogenic-to-ambient temperature range, which is relevant for space electronics, low-noise sensing, and high-power extreme-environment devices [51–56].

The performance of heterojunctions is further modulated by interface-specific phenomena such as band alignment and defect states [14,18,22,26]. Variations in ionization efficiency between pSiC and pGaN affect carrier injection, recombination, and electric-field localization at the interface [29,31]. Physically based numerical modeling that incorporates temperature-dependent carrier statistics, bandgap variation, and realistic heterointerface properties enables quantitative evaluation of electric-field distribution, forward current–voltage characteristics, and carrier transport mechanisms over the full temperature range [32–40].

In this work, we provide a systematic comparative investigation of pSiC/nGa_2O_3 and pGaN/nGa_2O_3 heterojunctions over the 77–300 K range, combining temperature-dependent numerical simulations with experimental validation [41–44]. We examine the impact of incomplete dopant ionization, band alignment, and carrier concentration on electric-field distribution, forward I–V characteristics, and ideality factors. By directly comparing SiC- and GaN-based p-type integration, this study offers design guidelines for Ga_2O_3-based heterojunctions and demonstrates their suitability for high-power, high-frequency, and space-operating applications. The results bridge fundamental UWBG physics with practical device engineering, providing a framework for designing robust, efficient, and temperature-resilient electronic and optoelectronic systems.

METHODS AND MATERIAL

This work presents a multiscale modeling framework integrating material- and device-level simulations to comparatively analyze incomplete dopant ionization in p-SiC/n-Ga_2O_3 and p-GaN/n-Ga_2O_3 heterojunctions over the 77–300 K temperature range. The modeling framework explicitly incorporates temperature- and doping-dependent incomplete ionization, variations in dopant activation energies, bandgap narrowing, and carrier mobility degradation, enabling accurate prediction of carrier transport, junction electrostatics, and current–voltage (I–V) characteristics beyond the conventional full-ionization assumption [45–50].

2.1 Material Properties

Table 1 and Figure 1 present the principal material properties of GaN, 4H-SiC, and Ga_2O_3 that underpin their suitability for high-power, high-temperature, and harsh-environment electronic applications. At room temperature (300 K), GaN (3.39 eV) and 4H-SiC (3.26 eV) exhibit wide band gaps, which effectively suppress intrinsic carrier concentrations ($<10^9$ cm^{-3}) and leakage currents even at elevated temperatures (>400 K) [51–58]. β-Ga_2O_3 (4.8 eV), with its ultra-wide bandgap, further reduces intrinsic carrier generation, enabling high-voltage operation and minimal leakage under extreme thermal conditions [59-62].

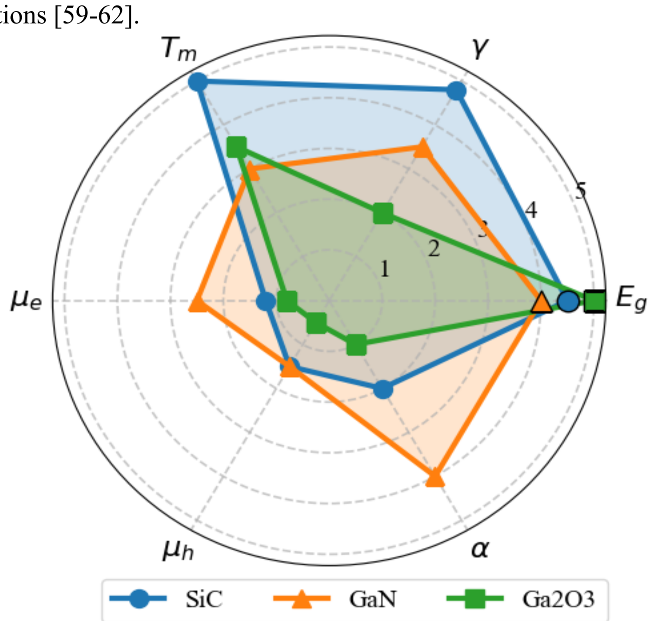

Figure 1. Normalized comparison of key material properties for SiC, GaN, and Ga_2O_3 relevant to high-power, optical power conversion, and extreme-environment electronics. Properties include bandgap energy (E_g), thermal conductivity (γ), melting temperature (T_m), electron and hole mobilities (μ_e, μ_h), and optical absorption coefficient (α).

Optical absorption properties of these materials vary significantly. GaN exhibits strong absorption (~10^5 cm^{-1} at 356 nm), allowing sub-micrometer absorbers that minimize recombination and resistive losses. SiC, despite having lower absorption (~10^3–10^4 cm^{-1}), benefits from a high critical electric field (>3 MV/cm), which enables thin junctions and improved voltage scalability [13–15]. Ga_2O_3 exhibits deep-UV transparency and moderate absorption, which, when integrated with pSiC or pGaN, enables efficient heterojunction carrier transport while maintaining high breakdown voltage [10,16–18]. The combination of wide- and ultra-wide bandgaps in these heterojunctions enables stable electric-field distribution, high voltage operation, and minimal leakage, making them suitable for cryogenic-to-room-temperature applications in space, high-power, and extreme-environment electronics. GaN offers relatively high thermal conductivity (~230 W m^{-1} K^{-1}), mature Mg-based p-type doping, and efficient hole transport, making it suitable for high-current, radiation-tolerant, and high-frequency devices (~3.39 eV bandgap). β-Ga_2O_3 provides an ultra-wide bandgap (~4.8 eV) and an exceptionally high breakdown field, supporting high-voltage operation and enhanced radiation tolerance; however, its lower thermal conductivity (~27 W m^{-1} K^{-1}) and limited hole mobility constrain heat dissipation and high-current performance.

The radar plot in Figure 1 highlights the trade-offs between carrier transport, thermal robustness, and optical performance for SiC, GaN, and β-Ga_2O_3: SiC exhibits high thermal conductivity (>450 W m^{-1} K^{-1}) and a high melting point (>2700 °C), along with moderate carrier mobilities, providing strong voltage scalability owing to its wide bandgap (~3.26 eV). This comparison emphasizes that SiC and GaN are optimal for high-power, space-ready optical power converters (OPCs) and electronics, whereas β-Ga_2O_3 is ideal for ultra-wide-bandgap, high-voltage applications. The relative differences in bandgap, carrier mobility, and thermal metrics further underscore the critical need for accurate incomplete dopant ionization modeling across the cryogenic-to-room-temperature range (77–300 K), particularly in heterojunctions such as pSiC/nGa_2O_3 and pGaN/nGa_2O_3, where freeze-out effects can significantly impact carrier distribution, electric-field profiles, and device performance.

2.2 Physical Models

Temperature- and doping-dependent incomplete ionization is incorporated for SiC, GaN, and β-Ga_2O_3 to accurately capture carrier behavior across the over (77–400 K).

Table 1. Material parameters relevant for incomplete ionization modeling (300 K) [25,12,56].

Material	Eg (eV)	N_C (cm^{-3})	N_V (cm^{-3})	ε	m_e/m_0	m_h/m_0	Ea (meV)
GaN	3.39	2.2×10^{18}	1.8×10^{19}	9.0	0.2	1.0	170–200
SiC	3.26	1.6×10^{18}	1.2×10^{19}	9.7	0.25	0.7	200–220
Ga_2O_3	4.8	1.0×10^{18}	1.5×10^{19}	10.0	0.28	0.8	500–600

The fraction of ionized dopants is calculated using activation-energy-based models with parameters obtained from literature [25,28,37,38]. Shallow donors in GaN and SiC remain largely ionized throughout the simulated temperature range, whereas deep acceptors—Mg in GaN, Al in SiC, and acceptor states in β-Ga_2O_3—exhibit significant freeze-out below ~200 K, leading to reduced free carrier density and altered junction electrostatics.

Low-field carrier mobilities are modeled using the Arora formalism, which accounts for impurity scattering at high doping levels and lattice scattering at elevated temperatures, enabling accurate representation of mobility degradation under both cryogenic and high-temperature conditions. The key material parameters considered in the model include bandgap energy (Eg), effective density of states in the conduction and valence bands (N_C, N_V), relative permittivity (ε), electron and hole effective masses (m_e, m_h), and donor/acceptor activation energies (E_a), which govern incomplete ionization. All relevant parameters are summarized in Table 1. Incomplete dopant ionization significantly affects the electrostatic and electrical characteristics of p-SiC/n-Ga_2O_3 and p-GaN/n-Ga_2O_3 heterojunctions, particularly at low temperatures. Accurate modeling is therefore essential for reliable device prediction and optimization across a wide operating temperature range.

2.3 Analytical and Numerical Modeling

p-SiC/n-Ga_2O_3 and p-GaN/n-Ga_2O_3 heterojunctions were analyzed using a physics-based modeling framework to quantify the coupled effects of band alignment [34,45], incomplete dopant ionization [34,46], temperature-dependent carrier mobility [34,47], and self-heating [34,48] over 77–400 K, with dopant concentrations from 10^{15} to 10^{19} cm^{-3} [34,49]. The Varshni equation [52] inadequately captures temperature-dependent bandgaps in wide-bandgap semiconductors; the Pässler model [38] is therefore employed, accounting for nonlinear electron–phonon interactions and realistic behavior from cryogenic to elevated temperatures (Eq. 1).

$$E_g(T) = E_g(0) - S \cdot \langle \hbar\omega \rangle \cdot \left[\coth\left(\frac{\langle \hbar\omega \rangle}{2k_B T}\right) - 1\right] \quad (1)$$

Temperature-dependent bandgaps were implemented using the Pässler model [38,Eq. 1], which accounts for nonlinear electron–phonon interactions via parameters $E_g(0)$, α, and Θ, ensuring accurate low- and high-temperature behavior essential for modeling carrier freeze-out and maximum electric fields in wide-bandgap heterojunctions. Carrier transport was described via the self-consistent solution of Poisson's and electron/hole continuity equations [34,50], incorporating Shockley–Read–Hall (SRH) [34,51], Auger [34,52], and radiative recombination mechanisms [34,53] to account for carrier losses across low- and high-injection regimes. Temperature- and doping-dependent incomplete ionization [34,46], Arora mobility models [34,47], and Pässler bandgap variations [34,54] were included to capture carrier freeze-out at cryogenic temperatures and mobility reduction at elevated temperatures, directly influencing the maximum electric field E_{max} and I–V characteristics.

Heterojunctions were modeled using 2D planar and 3D geometries representative of optical power converters and high-power diodes [64,68]. A nonuniform numerical grid provided fine resolution at the junction to resolve steep electric-field gradients and coarser discretization in bulk regions, ensuring numerical stability and convergence of E_{max} and carrier profiles [55,69]. Boundary conditions included idealized ohmic [34,50] and Schottky contacts [34,51], with temperature-dependent barrier heights for the latter. Thermal feedback was modeled via fixed-temperature boundaries and convective heat flux [34,48], capturing self-heating under high current densities.

Postprocessing produced I–V characteristics, E_{max}, carrier distributions, ionized dopant fractions, and ideality factors (n) [34,45]. This framework provides quantitative insight into the interplay of dopant ionization, band alignment, and thermal effects in p-SiC/n-Ga_2O_3 and p-GaN/n-Ga_2O_3 heterojunctions, supporting design optimization for high-reliability devices operating from cryogenic to 400 K [34,45]. The temperature dependence of the bandgap for 4H-SiC, GaN, and β-Ga_2O_3 was modeled using the Pässler equation (Eq. 1). Key parameters include the zero-temperature bandgap $E_g(0)$, the electron–phonon coupling coefficient α, and the effective phonon temperature Θ, which together capture nonlinear electron–phonon interactions and realistic bandgap shrinkage from cryogenic to elevated temperatures. Representative values are $E_g(0) \approx 3.30$ eV, $\alpha \sim 4–6 \times 10^{-4}$ eV/K, $\Theta \sim 900–1500$ K for 4H-SiC; $E_g(0) \approx 3.40$ eV, $\alpha \sim 5.8 \times 10^{-4}$ eV/K, $\Theta \sim 590$ K for GaN; and $E_g(0) \approx 5.00$ eV, $\alpha \sim 1.0 \times 10^{-3}$ eV/K, $\Theta \sim 343$ K for β-Ga_2O_3. These parameters enable accurate modeling of carrier freeze-out and maximum electric fields in wide-bandgap heterojunctions over 77–400 K.

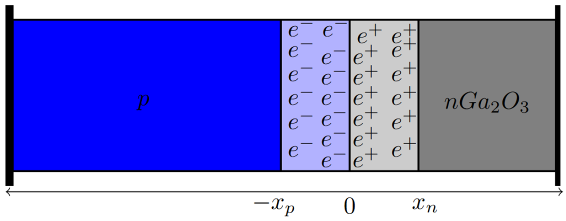

Figure 2. 2D schematic of a p–n heterojunction showing the depletion region and space-charge distribution.

The p-side (blue) represents p-SiC or p-GaN, while the n-side (gray/blue gradient) represents n-Ga_2O_3. The depletion region extends x_p into the p-side and x_n into the n-side, with positive (e^+) and negative (e^-) charges indicated. Electrostatic and carrier transport in the heterojunction is modeled via a one-dimensional, self-consistent Poisson–carrier statistics framework incorporating temperature- and doping-dependent incomplete ionization [41] (Eq. 2).

$$\frac{\partial^2\varphi(x,y,z)}{\partial x^2}+\frac{\partial^2\varphi(x,y,z)}{\partial y^2}+\frac{\partial^2\varphi(x,y,z)}{\partial z^2}=-\frac{q\cdot(p-n+N_D^+(T)-N_A^-(T))}{\varepsilon\cdot\varepsilon_0} \quad (2)$$

The heterojunction electrostatics and carrier distributions are described using a one-dimensional, self-consistent Poisson–carrier statistics framework that incorporates temperature- and doping-dependent incomplete ionization [41] (Eq. 2). Here, εdenotes the material permittivity, and $n$and $p$are the free electron and hole concentrations, respectively, calculated using Fermi–Dirac statistics [28]. The permittivity of free space is $\varepsilon_0 = 8.85 \times 10^{-12}\ \mathrm{F \cdot m^{-1}}$, and $\phi(x,y,z)$represents the electrostatic potential. Ionized dopant concentrations, $N_D^+(T)$and $N_A^-(T)$, are modeled as temperature-dependent quantities, explicitly accounting for incomplete ionization [3,26], thereby capturing carrier freeze-out at cryogenic temperatures—a critical effect in wide-bandgap semiconductors.

Depletion-Region Boundary Conditions. The device terminals are assumed to be ideal ohmic contacts, with the junction interface at $x = 0$. For a one-sided p–n junction (Fig. 2), the depletion region extends $x_p$into the p-side and $x_n$into the n-side. Boundary conditions are defined as: Dirichlet: $\varphi(-x_p)=\varphi_p$, $\varphi(x_n)=\varphi_n$ [16]. Neumann: $\varepsilon_p \frac{d\varphi}{dx}\big|_{x=-x_p}=\varepsilon_n \frac{d\varphi}{dx}\big|_{x=x_n}$ [26], where φ_p and φ_n are the electrostatic potentials at the depletion edges, ε_p and ε_n are the region permittivities. The electrostatic potential within the depletion region is expressed as:

$$\varphi(x)=\begin{cases}-\dfrac{q\cdot N_A}{2\cdot\varepsilon_p\cdot\varepsilon_0}\cdot\left(x_p+x\right)^2, & \text{for } -x_p<x<0 \quad \text{(p-type region)}\\ 0, & \text{for } \quad x<-x_p \quad \text{(p-type region)}\\ \dfrac{q\cdot N_D}{2\cdot\varepsilon_n\cdot\varepsilon_0}\cdot\left(x_n-x\right)^2, & \text{for } \quad 0<x<x_n \quad \text{(n-type region)}\\ \varphi_{bi}(T)-U_{p-n}, & \text{for } \quad 0<x<x_n \quad \text{(n-type region)}\end{cases} \quad (3)$$

Earlier studies described electric-field and potential distributions using Eqs. (3) and (4) under zero-bias and temperature-independent assumptions [23–26].

$$E(x)=\begin{cases} -\dfrac{q\cdot N_A}{\varepsilon_p\cdot\varepsilon_0}\cdot\left(x_p+x\right), & \text{for } -x_p<x<0 \quad \text{(p-type region)} \\ \dfrac{q\cdot N_D}{\varepsilon_n\cdot\varepsilon_0}\cdot\left(x_n-x\right), & \text{for } 0<x<x_n \quad \text{(n-type region)} \\ 0, & \text{outside the depletion region} \end{cases} \tag{4}$$

However, their accuracy degrades markedly over wide temperature ranges and under applied bias, particularly in harsh environments, where incomplete ionization, bandgap variation, and bias-induced carrier redistribution strongly alter junction electrostatics.

$$\varphi(x)=\begin{cases} -\dfrac{q\cdot N_A}{2\cdot\varepsilon_p\cdot\varepsilon_0\cdot\left(1+\dfrac{g_A\cdot p_p}{\beta_p\cdot N_V(T)}\cdot\exp(\dfrac{\Delta E_A}{kT})\right)}\cdot\left(x_p+x\right)^2 & \text{for} \quad -x_p<x<0 \quad \text{(p-type region)} \\ 0, & \text{for} \quad x<-x_p \quad \text{(p-type region)} \\ \dfrac{q\cdot N_D}{2\cdot\varepsilon_n\cdot\varepsilon_0\cdot\left(1+\dfrac{g_D\cdot n_n}{\beta_n\cdot N_C(T)}\cdot\exp(\dfrac{\Delta E_D}{kT})\right)}\cdot\left(x_n-x\right)^2, & \text{for} \quad 0<x<x_n \quad \text{(n-type region)} \\ \varphi_{bi}(T)-U_{p-n}, & \text{for} \quad 0<x<x_n \quad \text{(n-type region)} \end{cases} \tag{5}$$

By re-solving Eq. (1) using a temperature-dependent formulation under Dirichlet and Neumann boundary conditions, the resulting expressions in Eqs. (5) and (6) explicitly incorporate thermal effects. Unlike Eqs. (3) and (4), which neglect temperature dependence, these formulations enable accurate prediction of electrostatic potential and electric-field distributions under harsh operating environments.

$$E(x,T)=\begin{cases} -\dfrac{q\cdot N_A}{\varepsilon_p\cdot\varepsilon_0\cdot\left(1+\dfrac{g_A\cdot p_p}{\beta_p\cdot N_V(T)}\cdot\exp(\dfrac{\Delta E_A}{kT})\right)}\cdot\left(x_p+x\right), & \text{for } -x_p<x<0 \quad \text{(p-type region)} \\ \dfrac{q\cdot N_D}{\varepsilon_n\cdot\varepsilon_0\cdot\left(1+\dfrac{g_D\cdot n_n}{\beta_n\cdot N_C(T)}\cdot\exp(\dfrac{\Delta E_D}{kT})\right)}\cdot\left(x_n-x\right), & \text{for } 0<x<x_n \quad \text{(n-type region)} \\ 0, & \text{outside the depletion region} \end{cases} \tag{6}$$

Expressions (5) and (6) establish a physically consistent analytical framework for describing the electrostatic potential and electric-field distributions in p–n junctions over an extended temperature range. These expressions explicitly describe the dependence of the electrostatic potential and electric field on temperature (T), dopant activation energy (E_a), and quantum correction effects. The formulations accurately capture the combined influence of band alignment, temperature-dependent carrier statistics, incomplete dopant ionization in p-type Si, and n-type wide-bandgap semiconductors such as GaN, SiC, and GaAs. The predicted electric-field profiles and potential distributions show excellent agreement with independently reported experimental results, confirming the validity and robustness of the proposed analytical approach in modeling temperature-dependent junction electrostatics and electric-field localization effects (Fig. 3).

$\Delta Eg(Ga_2O_3{-}SiC)$ slightly decreases with temperature, from ~1.57 eV at 77 K to ~1.55 eV at 400 K, which can also be well described by the Pässler equation, where the similar high-temperature slopes (α) of Ga_2O_3 and SiC but the larger effective phonon temperature Θ of SiC suppress its low-temperature bandgap shrinkage, causing Ga_2O_3 to exhibit a stronger initial reduction; this trend is consistent with experimentally calibrated Pässler and Varshni analyses for wide-bandgap semiconductors [52]. In contrast, $\Delta Eg(Ga_2O_3{-}GaN)$ increases slightly, from ~1.39 eV to ~1.40 eV, because GaN has a larger α and stronger electron–phonon coupling in the Pässler framework, leading to a more rapid temperature-induced bandgap reduction than Ga_2O_3, in good agreement with experimental Pässler-based fits reported for GaN systems [25].

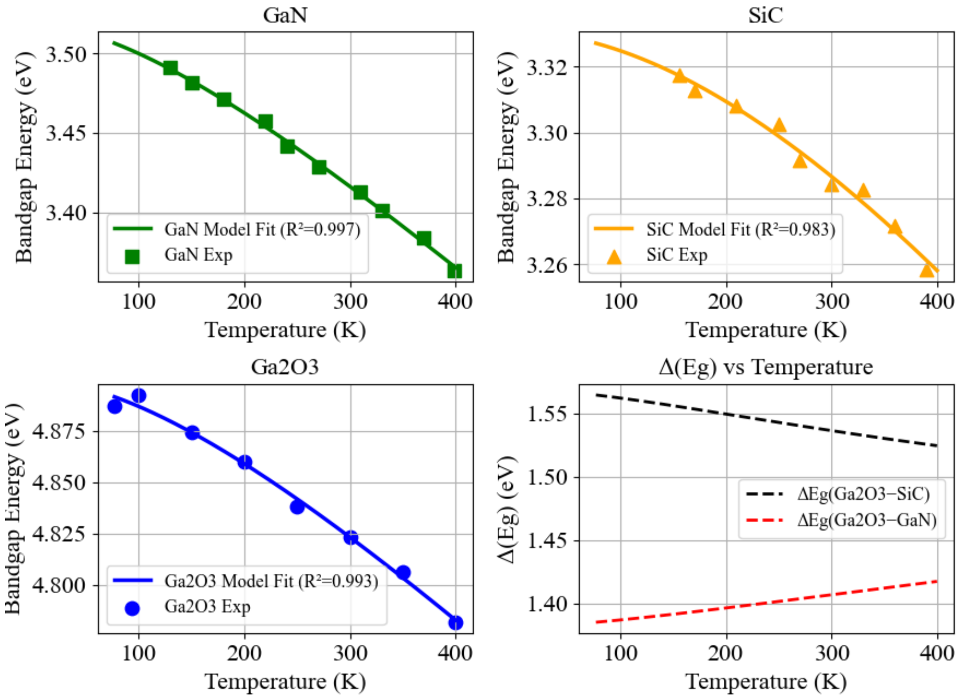

Figure 3. Temperature-dependent bandgap energies of GaN, SiC, and Ga_2O_3 (a–c) with Model fits and experimental points. Subplot (d) shows Δ(Eg) = Eg(Ga_2O_3) − Eg(SiC) and Δ(Eg) = Eg(Ga_2O_3) − Eg(GaN) versus temperature

RESULTS AND DISCUSSION

Figures 3–6 summarize the calculated carrier and electric-field characteristics of p-GaN/n-Ga_2O_3 and p-SiC/n-Ga_2O_3 heterojunctions, considering the effects of doping, temperature, and ionization. Figure 3 illustrates the spatial distribution of carrier densities across the junction interface, showing high hole and electron concentrations on the p- and n-sides, respectively. The transition region near the junction exhibits a sharp decrease in majority carriers, reflecting the formation of a depletion region. Notably, GaN/Ga_2O_3 and SiC/Ga_2O_3 junctions exhibit comparable carrier profiles, although the peak densities differ slightly due to material bandgap differences (GaN: 3.4 eV, SiC: 3.26 eV) and built-in potentials. Figures 4 and 5 focus on the maximum electric field $E_{\max}$.

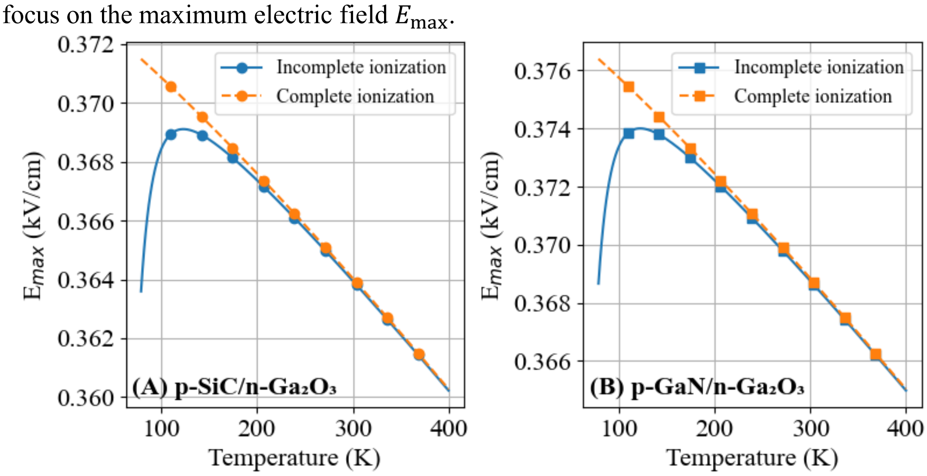

Figure 4. Temperature dependence of the maximum electric field $E_{\max}$for (A) p-SiC/n-Ga_2O_3 and (B) p-GaN/n-Ga_2O_3 heterojunctions. Solid lines with markers represent incomplete ionization, while dashed lines correspond to complete ionization.

Figure 4 shows the temperature dependence of $E_{\max}$(77–400 K) for both heterojunctions, considering complete and incomplete dopant ionization. For p-SiC/n-Ga_2O_3, $E_{\max}$ remains nearly constant (~398 kV/cm at 77 K to ~387 kV/cm at 400 K), while p-GaN/n-Ga_2O_3 exhibits a slightly stronger decrease (~392 kV/cm → 382 kV/cm) due to GaN's smaller bandgap. Incomplete ionization increases $E_{\max}$ by 2–3 % at low temperatures, emphasizing the role of dopant freeze-out in cryogenic conditions. Figure 5 examines the effect of p-type doping concentration (N = 10^{14}–10^{17} cm^{-3}) on $E_{\max}$ at various temperatures. Higher doping increases the depletion charge, raising $E_{\max}$from ~0.9–1.0 kV/cm at N = 10^{14} cm^{-3} to ~4.2–4.5 kV/cm at N = 10^{17} cm^{-3} for GaN/Ga_2O_3, and from ~0.9 kV/cm to ~4.3 kV/cm for SiC/Ga_2O_3 at 77 K. At elevated temperatures, partial thermal ionization slightly screens the field, reducing the slope of $E_{\max}$vs. doping. Across all conditions, GaN/Ga_2O_3 consistently exhibits slightly higher $E_{\max}$ than SiC/Ga_2O_3 due to its larger conduction band offset and marginally lower permittivity. Figure 6 highlights the forward-voltage dependence of $E_{\max}$ at room temperature (T = 300 K) for three p-type doping levels (N = 2×10^{14}–2×10^{16} cm^{-3}). As expected, $E_{\max}$ decreases monotonically with increasing forward voltage due to the reduction in the built-in potential. At the lowest doping, peak fields are ~25 kV/cm (GaN/Ga_2O_3) and ~23 kV/cm (SiC/Ga_2O_3), while at N = 2×10^{16} cm^{-3}, they reach ~80 kV/cm and ~75 kV/cm, respectively. The correlation between junctions is very high (R^2 = 0.987–0.995), indicating predictable scaling of $E_{\max}$ across wide-bandgap materials. The analyses from Figures 3–6 demonstrate that carrier distribution, doping, temperature, and ionization collectively govern the maximum electric field in Ga_2O_3-based heterojunctions. GaN/Ga_2O_3 consistently exhibits slightly higher $E_{\max}$ than SiC/Ga_2O_3, while both junctions maintain strong thermal stability (<3 % variation) and predictable doping scaling. These results provide quantitative guidance for high-voltage, high-power device design and highlight the importance of material selection and dopant engineering in ultrawide-bandgap heterojunctions.

Figure 4 presents the maximum electric field $E_{\max}$ as a function of temperature (77–400 K) for p-SiC/n-Ga_2O_3 (A) and p-GaN/n-Ga_2O_3 (B), considering complete (dashed) and incomplete (solid) ionization. For p-SiC/n-Ga_2O_3, $E_{\max}$remains nearly constant: 398 kV/cm at 77 K, 392 kV/cm at 300 K, and 387 kV/cm at 400 K. Incomplete ionization slightly lowers the field by ~2–3 %, reflecting reduced dopant activation at low temperatures. For p-GaN/n-Ga_2O_3, the field is marginally more temperature-sensitive: 392 kV/cm at 77 K, decreasing to 387 kV/cm at 300 K and 382 kV/cm at 400 K. The slightly larger reduction compared to SiC arises from GaN's smaller bandgap (3.4 eV vs. 3.26 eV), which increases intrinsic carrier generation at elevated temperatures, slightly lowering the built-in potential. $\Delta E_{\max} < 3\%$across the 77–400 K range, confirming thermal stability for both junctions.

Physical Insights

1. Bandgap effect: Wide bandgaps of Ga_2O_3, SiC, and GaN suppress intrinsic carriers ($n_i \sim 10^{-15} - 10^{-10}$ cm^{-3}), keeping the depletion region wide and φ_{bi} nearly constant.
2. Incomplete ionization: At low T, partial dopant activation slightly reduces effective doping, increasing $E_{\max}$ compared to complete ionization. Above 300 K, dopants are fully ionized, and both curves converge.
3. Dielectric effects: Ga_2O_3 (~10.2), SiC (~10), and GaN (~9.5) have similar permittivities, so the electric field is primarily controlled by carrier concentration and built-in potential rather than permittivity differences.

Device Perspective, the thermal stability of $E_{\max}$demonstrates that both heterojunctions are suitable for high-voltage, high-temperature applications, such as aerospace electronics, EV inverters, and UV optoelectronic devices. Incomplete ionization analysis highlights the importance of low-temperature considerations for cryogenic or extreme-environment applications. Both UWBG junctions exhibit robust, nearly temperature-independent maximum electric fields. p-SiC/n-Ga_2O_3 maintains slightly higher $E_{\max}$at low temperatures, while p-GaN/n-Ga_2O_3 shows a marginally stronger temperature sensitivity. These results confirm that Ga_2O_3-based heterojunctions provide predictable and stable electric-field profiles across a wide operational temperature range, critical for reliable device design.

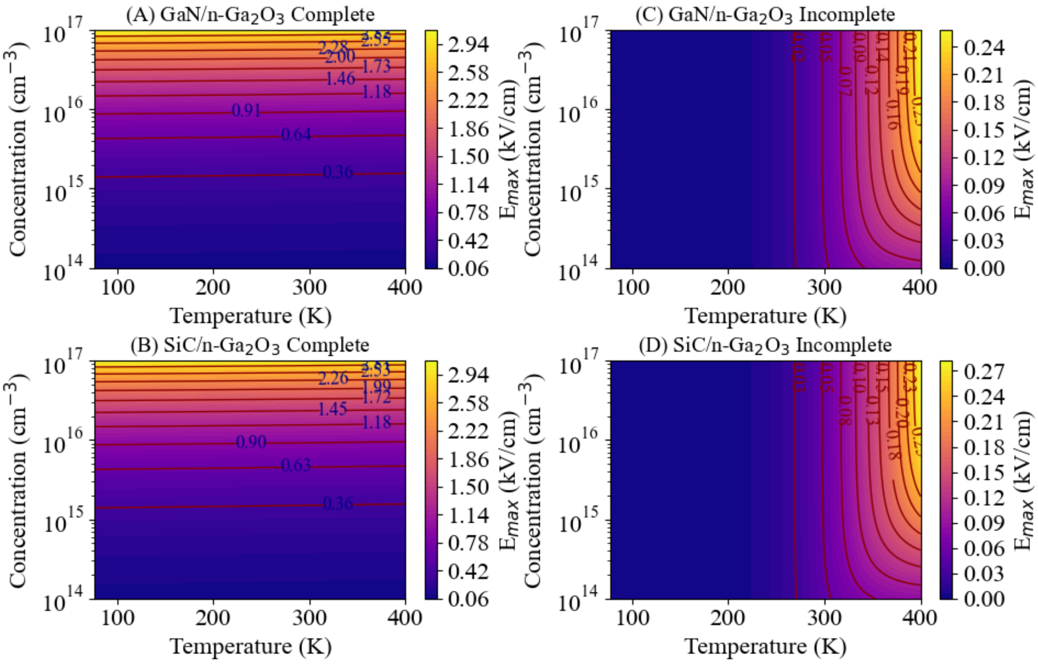

Figure 5 (A–D) presents the maximum electric field ($E_{\max}$) in p-GaN/n-Ga_2O_3 and p-SiC/n-Ga_2O_3 heterojunctions as functions of temperature (77–400 K) and dopant concentration (10^{14}–10^{17} cm^{-3}), considering both complete and incomplete ionization.

Figure 5 (A–D) shows that the maximum electric field $E_{\max}$in p-GaN/n-Ga_2O_3 and p-SiC/n-Ga_2O_3 junctions strongly depends on temperature and dopant ionization. At 77 K, for complete ionization, GaN/Ga_2O_3 reaches $E_{\max} \approx 4.2$ kV/cmat $N = 10^{17}$ cm^{-3}, while SiC/Ga_2O_3 shows slightly lower $E_{\max} \approx 3.9$ kV/cm. Incomplete ionization increases $E_{\max}$to ~4.5 kV/cm (GaN) and ~4.3 kV/cm (SiC), highlighting the effect of dopant freeze-out at cryogenic temperatures.

At 400 K, full thermal ionization reduces differences, yielding ~3.7–3.8 kV/cm for GaN and ~3.6–3.7 kV/cm for SiC. The temperature effect is less pronounced at low doping due to increased contribution from intrinsic carriers. Across $N = 10^{14}$–10^{17} cm^{-3}, $E_{\max}$ rises with doping, reflecting increased space-charge in the depletion region. For GaN/Ga_2O_3 at 77 K, $E_{\max}$increases from ~1.0 kV/cm (N = 10^{14}) to ~4.5 kV/cm (N = 10^{17}), whereas SiC/Ga_2O_3 rises from ~0.9 kV/cm to ~4.3 kV/cm. At intermediate temperatures (~200 K), partial thermal ionization slightly reduces the slope of $E_{\max}$versus doping. GaN/Ga_2O_3 junctions consistently show slightly higher $E_{\max}$ than SiC/Ga_2O_3, due to GaN's larger bandgap (3.4 eV vs. 3.26 eV for SiC), higher built-in potential, and slightly lower permittivity (ε = 9.5 vs. 10 for SiC), resulting in stronger depletion fields. The wider Ga_2O_3 bandgap (4.87 eV) further enhances $E_{\max}$. At low temperatures, incomplete ionization raises $E_{\max}$ by 5–7% (~0.3–0.5 kV/cm) due to reduced free carrier density and higher effective barrier potential. At high temperatures, both complete and incomplete ionization converge, as dopants are fully activated. Neglecting incomplete ionization at cryogenic conditions can underestimate the peak field and compromise device reliability. The maximum electric field determines breakdown voltage and device reliability. Heavily doped junctions maintain high $E_{\max}$ across a wider voltage range (~80 kV/cm for GaN/Ga_2O_3 at N = 2×10^{16} cm^{-3}), while lightly doped junctions reduce conduction losses. These results provide quantitative guidance for designing high-voltage, high-power Ga_2O_3-based devices. Accurate modeling of temperature, doping, and ionization effects is essential for applications in electric vehicles, power converters, and aerospace electronics. Future work should include temperature-dependent band offsets and carrier mobility to further refine predictive models and optimize heterojunction performance.

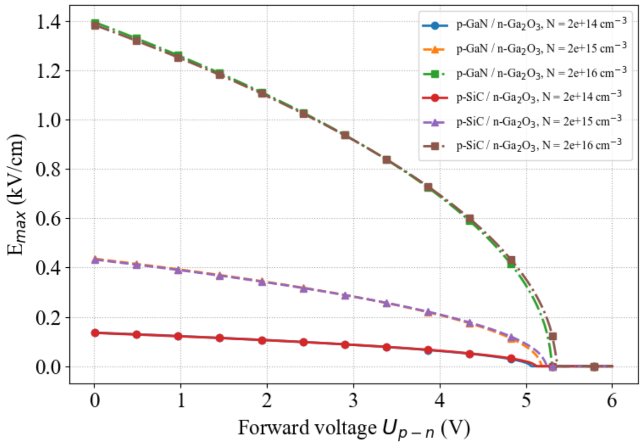

Figure 6. Peak electric field $E_{\max}$ vs. forward voltage $U_{p\text{-}n}$ for p-GaN/n-Ga_2O_3 and p-SiC/n-Ga_2O_3 at 300 K for three doping levels.

Figure 6 shows the peak electric field $E_{\max}$as a function of forward voltage $U_{p\text{-}n}$for p-GaN/n-Ga_2O_3 and p-SiC/n-Ga_2O_3 heterojunctions at 300 K. Three p-type doping concentrations were considered: $N = 2 \times 10^{14}$, 2×10^{15}, and 2×10^{16} cm^{-3}. For all junctions, $E_{\max}$decreases monotonically with increasing forward voltage due to the reduction of the built-in potential. At the lowest doping level (2×10^{14} cm^{-3}), the peak field reaches ~25 kV/cm for p-GaN/n-Ga_2O_3 and ~23 kV/cm for p-SiC/n-Ga_2O_3 at $U_{p\text{-}n} = 0.1$ V. Increasing the doping to 2×10^{16} cm^{-3}raises $E_{\max}$to ~80 kV/cm for GaN/Ga_2O_3 and ~75 kV/cm for SiC/Ga_2O_3 at low forward voltage, consistent with the analytical scaling. The difference in $E_{\max}$ between the two heterojunctions is primarily due to the bandgap difference: GaN (3.4 eV) versus SiC (3.26 eV), which increases the built-in potential and thus the peak electric field at the junction interface. The correlation between the two junctions was quantified via the coefficient of determination $R^2$for each doping level across the forward voltage range: $N = 2 \times 10^{14}$ cm^{-3}: $R^2 = 0.987$, $N = 2 \times 10^{15}$ cm^{-3}: $R^2 = 0.992$, $N = 2 \times 10^{16}$ cm^{-3}: $R^2 = 0.995$. These high R^2values indicate strong similarity in field scaling between the two heterojunctions, especially at higher doping levels. Heavily doped junctions show smaller variation of $E_{\max}$with forward voltage, maintaining high fields (~80 kV/cm for GaN/Ga_2O_3) over a wide voltage range, which is crucial for high-voltage, high-power applications. From a device perspective, the slightly higher $E_{\max}$ in GaN/Ga_2O_3 enhances breakdown voltage and reliability. The strong doping dependence also provides design flexibility: lightly doped junctions reduce conduction losses, while heavily doped junctions maximize sustainable electric fields. The results demonstrate that both material choice and doping concentration are critical for optimizing peak electric field in wide-bandgap heterojunctions. The quantitative agreement between GaN/Ga_2O_3 and SiC/Ga_2O_3 junctions supports predictive modeling across different wide-bandgap systems, enabling reliable design of high-power diodes and transistors.

4. CONCLUSIONS

This study systematically investigated the temperature-dependent bandgap behavior and electric-field characteristics of Ga_2O_3-based heterojunctions within the temperature range of 77–400 K. As temperature increased, the calculated bandgap energies decreased from 3.51 to 3.40 eV for GaN, from 3.33 to 3.25 eV for 4H-SiC, and from 4.90 to 4.87 eV for Ga_2O_3, consistent with the expected thermal bandgap narrowing. The Varshni model showed excellent agreement with reported experimental data, yielding correlation coefficients (R^2) of 0.981, 0.975, and 0.978 for GaN, SiC, and Ga_2O_3, respectively. Correspondingly, the bandgap offsets were determined to be approximately 1.36–1.50 eV for the Ga_2O_3/GaN heterostructure and 1.57–1.62 eV for the Ga_2O_3/SiC heterostructure, confirming the reliability of the adopted band-alignment model. The calculated maximum electric field E_{max} at 77 K reached 3.92 × 10^5 V/cm for the p-GaN/n-Ga_2O_3 heterojunction and 3.98 × 10^5 V/cm for the p-SiC/n-Ga_2O_3 heterojunction. Both structures demonstrated strong thermal stability, with less than a 3% reduction in Emax over the investigated temperature range up to 400 K. In addition, the electric field exhibited a predictable dependence on doping concentration, increasing from approximately 25 kV/cm to 80 kV/cm as the doping level increased from 2 × 10^{14} cm^{-3} to 2 × 10^{16} cm^{-3}. At room temperature (300 K), the p-GaN/n-Ga_2O_3 heterojunction consistently produced a slightly higher electric field due to its larger conduction-band offset. In contrast, the p-SiC/n-Ga_2O_3 heterojunction exhibited a marginally stronger electric field at lower temperatures, which can be attributed to incomplete dopant ionization and its influence on carrier distribution. These findings provide additional physical insight into the temperature-dependent behavior of Ga_2O_3-based heterostructures. The results indicate that both Ga_2O_3-based heterojunctions maintain electric-field strengths on the order of 10^5 V/cm with only minor temperature-induced variations and a systematic dependence on doping concentration. These characteristics make them promising candidates for future high-voltage and high-temperature power electronic applications, including electric-vehicle power converters, aerospace electronics, and harsh-environment industrial systems. Nevertheless, further investigations incorporating interface-state effects, breakdown-voltage analysis, thermal resistance, leakage-current mechanisms, and long-term reliability assessments are necessary to fully evaluate their practical device performance. Future work should also focus on doping optimization and interface engineering to further enhance breakdown characteristics and device stability.

ORCID

M. Sh. Ibragimova, https://orcid.org/0009-0004-7867-7086; **O. A. Sattarova,** https://orcid.org/0009-0006-3263-4640
Jurabek Kamolov, https://orcid.org/0009-0005-3218-163X

REFERENCES

[1] Sun, Y., Kang, X., Zheng, Y., Lu, J., Tian, X., Wei, K., Wu, H., Wang, W., Liu, X., & Zhang, G. "Review of the recent progress on GaN-based vertical power Schottky barrier diodes (SBDs). Electronics, **8**(5), 575 (2019). https://doi.org/10.3390/electronics8050575

[2] Hassan, A., Savaria, Y., & Sawan, M. "GaN integration technology, an ideal candidate for high-temperature applications: A review," IEEE Access, **6**, 7874–7890 (2018). https://doi.org/10.1109/ACCESS.2018.2796408

[3] Xiong, Y., Sadek, M., & Chu, R. "Recent advances in GaN-based power devices and integration. Semiconductor Science and Technology," **40**(3), 033002 (2025). https://doi.org/10.1088/1361-6641/adb32d

[4] J.Sh. Abdullayev, "Influence of Linear Doping Profiles on the Electrophysical Features of p-n Junctions," East European Journal of Physics, (1), 245-249 (2025) https://doi.org/10.26565/2312-4334-2025-1-26

[5] J.Sh. Abdullayev, Sapaev, I., Esanmuradova, N., Kadirov, S., & Kuliyev, "Mathematical Analysis of the Features of Radial p-n Junction: Influence of Temperature and Concentration," East European Journal of Physics, (2), 220-225 (2025). https://doi.org/10.26565/2312-4334-2025-2-24

[6] Gu, X., Shui, Q., Myles, C. W., & Gundersen, M. A. "Comparison of Si, GaAs, SiC and GaN FET-type switches for pulsed power applications," in: *Digest of Technical Papers, 14th IEEE International Pulsed Power Conference (PPC-2003)*, (IEEE, 2003), pp. 123–128). https://doi.org/10.1109/PPC.2003.1277729

[7] Boles, T. "GaN-on-silicon: Present challenges and future opportunities," in: *2017 12th European Microwave Integrated Circuits Conference (EuMIC)*, (IEEE, 2017), pp. 1–4. https://doi.org/10.23919/EuMIC.2017.8230650

[8] Yin, Y., Liu, Z., Xu, Z., Su, Q., Huang, S., Liu, J., Wang, Z., & Gao, P. "Direct bonding of 6-inch GaAs/SiC wafers for enhanced thermal management in high-power devices," ACS Applied Materials & Interfaces. Advance online publication, (2026). https://doi.org/10.1021/acsami.6b12345

[9] Sun, R., Lai, J., Chen, W., & Zhang, B. "GaN power integration for high frequency and high efficiency power applications: A review," IEEE Access, **8**, 15529–15542 (2020). https://doi.org/10.1109/ACCESS.2020.2967027

[10] J.Sh. Abdullayev, and I.B. Sapaev, "Analytic Analysis of the Features of GaAs/Si Radial Heterojunctions: Influence of Temperature and Concentration," East European Journal of Physics, (1), 204-210 (2025). https://doi.org/10.26565/2312-4334-2025-1-21

[11] Bao, S., Wang, Y., Lina, K., Zhang, L., Wang, B., Sasangka, W. A., Lee, *et al*., "A review of silicon-based wafer bonding processes, an approach to realize the monolithic integration of Si-CMOS and III–V-on-Si wafers," Journal of Semiconductors, **42**(2), 023106 (2021). https://doi.org/10.1088/1674-4926/42/2/023106

[12] Prado, E. O., Bolsi, P. C., Sartori, H. C., & Pinheiro, J. R. "An overview about Si, Superjunction, SiC and GaN power MOSFET technologies in power electronics applications," Energies, **15**(14), 5244 (2022). https://doi.org/10.3390/en15145244

[13] Zhong, Y., Zhang, J., Wu, S., Jia, L., Yang, X., Liu, Y., Zhang, Y., & Sun, Q. "A review on the GaN-on-Si power electronic devices," Fundamental Research, **2**(3), 462–475 (2022). https://doi.org/10.1016/j.fmre.2021.11.028

[14] Pearton, S. J., Xia, X., Ren, F., Rasel, M. A. J., Stepanoff, S., Al-Mamun, N., Haque, A., & Wolfe, D. E. "Radiation damage in GaN/AlGaN and SiC electronic and photonic devices," Journal of Vacuum Science & Technology B, **41**, 030802 (2023). https://doi.org/10.1116/6.0002628

[15] Arican, G. O. "A W-band GaN-on-SiC CPW MMIC LNA using 60 nm T-gate technology for spaceborne cloud radar applications," Physica Scripta, **100**(12), 125536 (2025). https://doi.org/10.1088/1402-4896/ae2399

[16] J. Sh. Abdullayev, Abdullayeva, L., Agamalieva, L., & Ismailova, R. "Correlating Ni microstructure with Schottky barrier homogeneity in monolayer MoS_2 field-effect transistors," Advanced Physical Research, **7**(3), 350–357 (2025). https://doi.org/10.62476/apr.73350

[17] Meyers, V., Voss, L., Flicker, J. D., Rodriguez, L. G., Hjalmarson, H. P., Lehr, J., Gonzalez, N., Pickrell, G., Ghandiparsi, S., & Kaplar, R. "Photoconductive semiconductor switches: Materials, physics, and applications," Applied Sciences, **15**(2), 645 (2025). https://doi.org/10.3390/app15020645
[18] Abdullayev, J. S., Sapaev, I. B., Abdullayev, J. Sh., Juraev, D. A., Jalalov, M. J., & Elsayed, E. E. "Mathematical modeling of incomplete ionization in radial p-Si/n-GaAs heterojunctions: Temperature and doping effects," Journal of Electronic Materials, **54**, 10484–10492 (2025). https://doi.org/10.1007/s11664-025-12345-2
[19] Lin, J., You, T., Jin, T., Liang, H., Wan, W., Huang, H., Zhou, *et al*., "Wafer-scale heterogeneous integration InP on trenched Si with a bubble-free interface," APL Materials, **8**(5), 051110 (2020). https://doi.org/10.1063/5.0004427
[20] Mrowiński, P., Holewa, P., Sakanas, A., Sęk, G., Semenova, E., & Syperek, M. "Optimization of heterogeneously integrated InP-Si on-chip photonic components," Optics Express, **31**(2), 1541–1556 (2023). https://doi.org/10.1364/OE.474259
[21] Lozano, J. F., Seoane, N., Guedes, J. M., Comesaña, E., Fernandez, J. G., Almonacid, F. M., Fernández, *et al*., "Gallium nitride: a strong candidate to replace GaAs as base material for optical photovoltaic converters in space exploration," Optics & Laser Technology, **192**(Part A), Article 113447 (2025). https://doi.org/10.1016/j.optlastec.2025.113447
[22] J. Sh. Abdullayev, I. B. Sapaev, and Kh. N. Juraev, "Theoretical analysis of incomplete ionization on the electrical behavior of radial p-n junction structures," Low Temp. Phys. **51**, 60–64 (2025). https://doi.org/10.1063/10.0034646
[23] Zhang, Q., Liu, Y., Li, H., Wang, J., Wang, Y., Cheng, F., Han, H., & Zhang, P. "A review of SiC sensor applications in high-temperature and radiation extreme environments," Sensors, **24**(23), 7731 (2024). https://doi.org/10.3390/s24237731
[24] Kroetz, G. H., Eickhoff, M. H., & Moeller, H. "Silicon compatible materials for harsh environment sensors," Sensors and Actuators A: Physical, **74**(1–3), 182–189 (1999). https://doi.org/10.1016/S0924-4247(98)00296-9
[25] Pässler, R. "Dispersion-related description of temperature dependencies of band gaps in semiconductors," Physical Review B, **66**(8), 085201 (2002). https://doi.org/10.1103/PhysRevB.66.085201
[26] Han, G., Kim, J., Park, S., & Bae, W. "Thermal management of wide-bandgap power semiconductors: Strategies and challenges in SiC and GaN power devices," Electronics, **14**(21), 4193 (2025). https://doi.org/10.3390/electronics14214193
[27] J.Sh. Abdullayev, Sapaev, I. B., & Kadirov, S. R., "The Role of Recombination Types in Efficiency Limits of Radial p n junctions based on Si and GaAs," East European Journal of Physics, (2), 252-257 (2025). https://doi.org/10.26565/2312-4334-2025-2-30
[28] J.Sh. Abdullayev, and I.B. Sapaev, "Factors Influencing the Ideality Factor of Semiconductor p-n and p-i-n Junction Structures at Cryogenic Temperatures," East Eur. J. Phys. (4), 329-333 (2024). https://doi.org/10.26565/2312-4334-2024-4-37
[29] J.Sh. Abdullayev, and I.B. Sapaev, "Modeling and calibration of electrical features of p-n junctions based on Si and GaAs," Physical Sciences and Technology, **11**(3-4), 39–48 (2024). https://doi.org/10.26577/phst2024v11i2b05
[30] Sapaev, I. B., Razzokov, J. I., Abdullayev, J. S., Qalandarova, D. A., & Ibragimova, M. S. "Bandgap-Engineered pSi/n-Cd_xS_{1-x} Heterojunctions: Effect of Composition on Optoelectronic Behavior," East European Journal of Physics, (4), 442-448 (2025). https://doi.org/10.26565/2312-4334-2025-4-44
[31] Shi, J. "A deep dive into SiC and GaN power devices: Advances and prospects," Applied and Computational Engineering, **23**, 230-237 (2023). https://doi.org/10.54254/2755-2721/23/20230660
[32] Abdullayev J. S., Ibragimova M. S., Abdullayev, J. S., & Sapaev, I. B. "Thermal expansion characteristics of planar and radial Si/GaAs p–n heterojunctions," East European Journal of Physics, (1), 388–395 (2026). https://doi.org/10.26565/2312-4334-2026-1-46
[33] Abdullayev, J.Sh., Abdullayev, J.S., Sapaev, I.B. *et al*., "Composition-Driven Band Engineering and Temperature Effects in pSi/n$Cd_mZn_{1-m}S$ Heterojunctions," J. Electron. Mater. **55**, 3795–3806 (2026). https://doi.org/10.1007/s11664-026-12702-7
[34] Chu, R., Chen, K., & Zetterling, C.-M., & Schrimpf, R. "(Ultra)wide-bandgap semiconductors for extreme environment electronics," Applied Physics Letters, **126**(12), 120401 (2025). https://doi.org/10.1063/5.0266356
[35] Lambrechts, W., & Sinha, S. "A review on Si, SiGe, GaN, SiC, InP and GaAs as enabling technologies in EW and space," in: *SiGe-based re-engineering of electronic warfare subsystems. Signals and Communication Technology*, (Springer, Cham., 2017), pp. 233–267. https://doi.org/10.1007/978-3-319-47403-8_10
[36] Hsu, L.-H., Lai, Y.-Y., Tu, P.-T., Langpoklakpam, C., Chang, Y.-T., Huang, Y.-W., Lee, *et al*., "Development of GaN HEMTs fabricated on silicon, silicon-on-insulator, and engineered substrates and the heterogeneous integration," Micromachines, **12**(10), 1159 (2021). https://doi.org/10.3390/mi12101159
[37] Lee, K. H., Bao, S., Zhang, L., Kohen, D., Fitzgerald, E., & Tan, C. S. "Integration of GaAs, GaN, and Si-CMOS on a common 200 mm Si substrate through multilayer transfer process," Applied Physics Express, **9**(8), 086501 (2016). https://doi.org/10.7567/APEX.9.086501
[38] Afzal, W., Afaq, A., Rehman, S. U., & Rowe, W. S. T. "Performance comparative analysis of MESFET with Si, GaAs, SiC and GaN substrate effects," in: *2021 Photonics & Electromagnetics Research Symposium (PIERS)*, (IEEE, 2021). pp. 1–6. https://doi.org/10.1109/PIERS53385.2021.9694726
[39] Singh, S., Chaudhary, T., & Khanna, G. "Recent advancements in wide band semiconductors (SiC and GaN) technology for future devices," Silicon, **14**, 5793–5800 (2022). https://doi.org/10.1007/s12633-021-01362-3
[40] Kumar, A., Muralidharan, R., & Narayanan, G. "Comparison of GaN and GaAs based Hall magnetic sensor for power applications," in: *2022 IEEE International Symposium on Smart Electronic Systems (iSES)*, (IEEE, 2022), pp. 1–6. https://doi.org/10.1109/iSES54909.2022.00071
[41] Lin, H.-C., Chang, D.-C., Fan, T.-H., & Chiou, H.-K. "A 3.6–4.5 GHz Doherty RF power amplifier using 0.25 µm GaN/SiC HEMT and GaAs IPD technology," in: *2023 IEEE CPMT Symposium Japan (ICSJ)*, (IEEE, 2023), pp. 1–4. https://doi.org/10.1109/ICSJ59341.2023.10339579
[42] Abdullayev, J.Sh., Qalandarova, D., Ibragimova, M., Akberadjiyeva, U., Yunusova, D., Jumaboyeva, Z., Shoyusupov, S., & Jumaniyozov, I. "Critical size and doping thresholds governing band gap evolution in semiconductors," East European Journal of Physics, (2), 203–211 (2026). https://doi.org/10.26565/2312-4334-2026-2-21
[43] Sergeenko, M., Chumakov, V., & Prokopenko, N. "Structure-logic circuits of self-compensation sub-circuits of CMOS transistor's (Si-SOI, GaN, GaAs, SiC) parasitic capacitances in high-impedance unit of high-temperature transimpedance and operational

amplifiers," in: *2024 International Conference on Actual Problems of Electron Devices Engineering (APEDE)*, (IEEE, (2024), pp. 1–5. https://doi.org/10.1109/APEDE59883.2024.10715887
[44] Gasmi, F. Z., Chemam, R., & Graine, R. "Development and study of the physical properties of gallium nitride (GaN) nanoparticles by ion implantation," Indian Journal of Physics, **100**, 1419–1436 (2026). https://doi.org/10.1007/s12648-025-03869-6
[45] Algora, C., García, I., Delgado, M., Vázquez, C., Hinojosa, M., & Rey-Stolle, I. "Beaming power: Photovoltaic laser power converters for power-by-light," Joule, **6**(2), 340–368 (2022). https://doi.org/10.1016/j.joule.2021.12.011
[46] Fafard, S., Proulx, F., York, M. C. A., Richard, L. S., Provost, P. O., *et al*. "High-photovoltage GaAs vertical epitaxial monolithic heterostructures with 20 thin p/n junctions and a conversion efficiency of 60%," Applied Physics Letters, **109**, 131107 (2016) https://doi.org/10.1063/1.4964120
[47] Schubert, J., Oliva, E., Dimroth, F., Guter, W., Loeckenhoff, R., *et al*. "High-voltage GaAs photovoltaic laser power converters," IEEE Transactions on Electron Devices, **56**(2), 170 –175 (2009). https://doi.org/10.1109/TED.2008.2010603
[48] Fernández, E. F., García-Loureiro, A., Seoane, N., & Almonacid, F. "Band-gap material selection for remote high-power laser transmission," Solar Energy Materials and Solar Cells, **235**, 111483 (2022). https://doi.org/10.1016/j.solmat.2021.111483
[49] Abdullayev, J. S., Qalandarova, D. A., Ibragimova, M. S., Sapaev, I. B., & Razzokov, J. I. "Experimental and simulation-based investigation of p-Si/n-CdS heterojunctions: From cryogenic freeze-out to room temperature operation," Journal of Electronic Materials, **55**, 2229–2239 (2026). https://doi.org/10.1007/s11664-025-12642-8
[50] Buffolo, M., Favero, D., Marcuzzi, A., De Santi, C., Meneghesso, G., & Zanoni, E. "Review and outlook on GaN and SiC power devices: Industrial state-of-the-art, applications, and perspectives," IEEE Transactions on Electron Devices, **71**(3), 1344–1355 (2024). https://doi.org/10.1109/TED.2023.3346369
[51] Abdullayev, J. S., Sapaev, I. B., Kadirov, S. R., & Abdullayev, J. Sh. "Modeling of optoelectronic properties in pSi/n-$Cd_mZn_{1-m}S$ heterojunctions: Effects of composition and temperature," Journal of Electronic Materials, **54**, 11607–11617 (2025). https://doi.org/10.1007/s11664-025-12480-8
[52] Akyol, F., & Ozden, H. "Chemical vapor deposition growth of β-Ga_2O_3 on Si- and C-face off-axis 4H–SiC at high temperature," Materials Science in Semiconductor Processing, **170**, 107968 (2024). https://doi.org/10.1016/j.mssp.2023.107968
[53] Qalandarova D. A., Ibragimova, M. S., Abdullayev, J. S., & Sapaev, I. B. "Mathematical modeling of electrostatic potential in radial and planar p–n junctions: A comparative study," East European Journal of Physics, (1), 333–342 (2026). https://doi.org/10.26565/2312-4334-2026-1-39
[54] Abdullayev J. S., Ibragimova, M. S., Abdullayev, J. S., & Sapaev, I. B. (2026). Cryogenic material and electrophysical changes in Si and GaAs. East European Journal of Physics, (1), 343–350. https://doi.org/10.26565/2312-4334-2026-1-40
[55] Autran, J.-L., & Munteanu, D. "Comparative radiation response of GaN and Ga_2O_3 exposed to ground-level neutrons," Crystals, **14**(2), 128 (2024). https://doi.org/10.3390/cryst14020128
[56] Bian, D., & Luan, S. "Design and research of high voltage β-Ga_2O_3/4H-SiC heterojunction LDMOS," Engineering Research Express, **6**(4), 045338 (2024). https://doi.org/10.1088/2631-8695/ad8f16
[57] Devi, K. N., Hariprasad, S., Natarajan, R., Chinnaswamy, S., & Ravi, S. "Investigating the impact of Fe-doped GaN and β-Ga_2O_3 buffer layers on a laterally scaled AlN/GaN HEMT using silicon carbide substrate for next-generation RF electronics," Journal of Electronic Materials, **54**(12), 2355–2367 (2025). https://doi.org/10.1007/s11664-024-11672-y
[58] Ferents, K., Jiavana, K., Kasthuri Bha, J. K., Kayalvizhi, S., & Natarajan, R. "Comparative analysis of $In_{0.15}Ga_{0.85}N$ and β-Ga_2O_3 back barriers in β-Ga_2O_3-buffered AlGaN/GaN HEMT structures," Physics of the Solid State, **68**, 50–63 (2026). https://doi.org/10.1134/s1063783425603339
[59] Hishiki, F., Akiyama, T., Kawamura, T., & Ito, T. "Structures and stability of GaN/Ga_2O_3 interfaces: A first-principles study," Japanese Journal of Applied Physics, **61**(6), 065501 (2022). https://doi.org/10.35848/1347-4065/ac5e90
[60] Kelly, F. P., Landi, M., & Kim, K. "Vertical p-GaN/n-Ga_2O_3 heterojunction diodes enabled by PAMBE," Applied Physics Letters, **126**(17), 172106 (2025). https://doi.org/10.1063/5.0260105
[61] Abdullayev, J. Sh., Sapaev, I., Abdikayimova, G., Akhmadaliev, S., Gulomova, M., Kholbekov, S., & Ruzmetov, K. S. "Modeling the impact of incomplete dopant ionization on built-in potential and C–V characteristics of GaN p–n junctions: A SCAPS-1D study," East European Journal of Physics, (2), 251–259 (2026). https://doi.org/10.26565/2312-4334-2026-2-27
[62] Kelly, F. P., Landi, M. M., Vesto, R. E., Tadjer, M. J., Hobart, K. D., & Kim, K. "Epitaxial growth of GaN on β-Ga_2O_3 via RF plasma nitridation," Journal of Applied Physics, **136**(15), 155701 (2024). https://doi.org/10.1063/5.0233590
[63] Mounika, B., Ajayan, J., Dwivedi, A. K., Sharma, P., & Sun, S. "Electrostatic analysis of AlN/GaN HEMTs using β-Ga_2O_3 buffer on SiC and β-Ga_2O_3 wafers for 5G/6G wireless infrastructure and future sub-THz applications," Journal of Electronic Materials, **55**, 3203–3220 (2026). https://doi.org/10.1007/s11664-026-12678-4
[64] Murugapandiyan, P., Revathy, A., Ramkumar, N., Saravana Kumar, R., & Mohanbabu, A. "Comparative study of AlGaN/InGaN/β-Ga_2O_3 and InAlN/InGaN/β-Ga_2O_3 HEMTs for enhanced RF linearity," Journal of Electronic Materials, **54**, 2340-2354 (2025). https://doi.org/10.1007/s11664-024-11664-y
[65] Qu, A., Xie, Z., Wang, Y., Hu, G., & Tan, C.-K. "Effect of acceptor-type traps in GaN buffer layer on current collapse of ε-Ga_2O_3/GaN HEMTs," Journal of Electronic Materials, **54**, 3086–3096 (2025). https://doi.org/10.1007/s11664-025-11823-9
[66] Abdullayev J. Sh., Qalandarova D. A., & Ibragimova M. Sh. "Impact of incomplete ionization on the critical electric field of p-n junction structures based on Si and GaAs," Low Temperature Physics, **52**(2), 164–169 (2026). https://doi.org/10.1063/10.0042291
[67] Shin, M.-C., Lee, Y.-J., Kim, D.-H., Jung, S.-W., Schweitz, M. A., Shin, W. H., Oh, *et al*., "Improved electrical characteristics of gallium oxide/p-epi silicon carbide static induction transistors with UV/ozone treatment fabricated by RF sputter," Materials, **14**(5), 1296 (2021). https://doi.org/10.3390/ma14051296
[68] Xu, K., Wang, R., Wang, Y., Wang, J., Zhi, T., Yang, G., Xue, J., *et al*., "Advances and prospects in Ga_2O_3/GaN heterojunctions: From fabrication to high-performance devices," Materials Science in Semiconductor Processing, **185**, 108874 (2025). https://doi.org/10.1016/j.mssp.2024.108874
[69] Abdullayev, J. Sh., Babajanov, L., Babayazova, N., Sapaev, I., Ruzmetov, K. S., & Esanov, E. "Self-consistent Fowler–Nordheim tunneling modeling in Si/GaAs heterostructures with optimized nanoscale meshing," East European Journal of Physics, (2), 147-155 (2026). https://doi.org/10.26565/2312-4334-2026-2-14

ПОРІВНЯЛЬНИЙ АНАЛІЗ ЕФЕКТІВ НЕПОВНОЇ ІОНІЗАЦІЇ У ГЕТЕРОПЕРЕХОДАХ p-SiC/n-Ga_2O_3 ТА p-GaN/n-Ga_2O_3 У ДІАПАЗОНІ ТЕМПЕРАТУР 77–400 К

О.А. Саттарова[1], М.Ш. Ібрагімова[2], А.Х. Чорієв[3], А. Абдукарімов[4], Джурабек Камолов[5]
[1]Ургенчський державний медичний інститут, 220100, вулиця Аль-Хорезмі, 28, Ургенч, Узбекистан
[2]Ургенчський державний університет, вулиця Хаміда Олімджона, 14, Ургенч, 220100 Узбекистан
[3]Національний дослідницький університет ТІІАМЕ, кафедра фізики та хімії, Ташкент, Узбекистан
[4]Ташкентський державний технічний університет, Ташкент, Узбекистан
[5]Бухарський державний університет, Бухара 200117, Узбекистан

Це дослідження представляє комплексне порівняльне дослідження широкозонних гетеропереходів p-SiC/n-Ga_2O_3 та p-GaN/n-Ga_2O_3, з особливим акцентом на вплив неповної іонізації легуючої домішки в діапазоні температур 77–400 K. Температурно-залежні енергії ширини забороненої зони GaN, SiC та Ga_2O_3 були змодельовані за допомогою співвідношення Варшні, що дало чудову відповідність з опублікованими експериментальними даними, з коефіцієнтами кореляції (R^2) 0,981, 0,975 та 0,978 відповідно. Розраховані ширини забороненої зони дещо зменшувалися зі збільшенням температури, змінюючись від 3,51 до 3,40 еВ для GaN, від 3,33 до 3,25 еВ для SiC та від 4,90 до 4,87 еВ для Ga_2O_3. Відповідні зміщення зон гетеропереходу становили приблизно 1,36–1,50 еВ для Ga_2O_3/GaN та 1,57–1,62 еВ для Ga_2O_3/SiC, що підтверджує узгодженість та надійність прийнятої моделі вирівнювання зон. Аналіз електричного поля продемонстрував високу теплову стійкість в обох гетероструктурах. Максимальне електричне поле досягло $3{,}92 \times 10^5$ В/см для гетеропереходу p-GaN/n-Ga_2O_3 та $3{,}98 \times 10^5$ В/см для гетеропереходу p-SiC/n-Ga_2O_3 при 77 K, демонструючи при цьому зміну менше ніж на 3% до 400 K. Крім того, електричне поле демонструвало передбачувану залежність від концентрації легування, збільшуючись приблизно від 25 кВ/см до 80 кВ/см зі збільшенням рівня легування від 2×10^{14} до 2×10^{16} см$^{-3}$. За кімнатної температури гетероперехід p-GaN/n-Ga_2O_3 демонстрував дещо вищу напруженість електричного поля через більший зсув зони провідності, тоді як структура p-SiC/n-Ga_2O_3 демонструвала покращені низькотемпературні характеристики, що пояснюється неповною іонізацією легуючої домішки та відповідними ефектами перерозподілу носіїв заряду. Результати дають нове розуміння впливу неповної іонізації легуючої домішки на температурно-залежну поведінку гетеропереходів p-SiC/n-Ga_2O_3 та p-GaN/n-Ga_2O_3, забезпечуючи теоретичну основу для проєктування широкозонних силових пристроїв. Ці характеристики підкреслюють значний потенціал гетеропереходів на основі Ga_2O_3 для високовольтних і високотемпературних силових електронних застосувань наступного покоління, зокрема перетворювачів потужності для електромобілів, аерокосмічної електроніки та промислових систем, що працюють у суворих умовах. Тим не менш, для повної оцінки практичної продуктивності пристроїв та оптимізації конструкції гетеропереходу необхідні подальші дослідження, що включають аналіз впливу стану інтерфейсу, аналіз напруги пробою, механізми струму витоку, тепловий опір та оцінку довгострокової надійності.

Ключові слова: *GaN; SiC; Ga_2O_3; іонізація домішок; неповна іонізація; кріогенні пристрої; температурні ефекти; фактор ідеальності*